A theoretical analysis for tube bulge forming using elastomer medium

Ramezani M. and Neitzert T.

Centre of Advanced Manufacturing Technologies (CAMTEC), School of Engineering, Auckland University of Technology, Auckland, New Zealand

Abstract

A new theoretical model is presented in this paper for bulge forming of tubular components with solid bulging mediums. The model is based on the results of the friction model which was developed previously by one of the authors for rubber/metal contact and takes into account the effect of local contact conditions. FE simulations using commercial software ABAQUS are carried out for an axisymmetric tube bulging operation using the defined friction model. The comparisons of the results of the theoretical model and the FE simulations clearly show that the newly developed theoretical model is suitable for predicting forming pressure and stress in the tube. The effect of key process parameters such as the friction between the tube and the die, the tube initial thickness and the length of the ealastomeric rod on the results are investigated using theoretical and FE models.

Keywords*: Finite element simulation; Friction; Theoretical analysis, Tube bulging.*

1 Introduction

In recent years, tube bulge forming techniques have been used in producing a wide range of tubular components. This is mainly due to the quest to decrease production costs and to optimize production technology. This technique is used for producing bicycle frame brackets from mild steel bulging and to manufacture the rear axle castings for automobiles. The process is also widely used in forming copper pipe fittings for domestic water and gas supplies [1].

The bulge forming of pipes can be done by implementing the internal hydrostatic pressure via a medium. The pressure medium is usually a liquid (hydraulic fluid or water) or solid elastomer (rubber or polyurethane). By restraining the pipe in dies with different geometries, components with desired shapes can be produced. Excessive thinning due to the high internal pressure is the main limitation of this process. To overcome this problem, compressive axial loading is applied to the end of the tube together with the internal pressure. In the bulge forming of tubes with solid medium, an elastomer rod inside the tube applies lateral pressure to expand the tube circumferentially, while simultaneous axial feeding of the tube is secured by the frictional traction on the tube as the elastomer rod deforms relative to the tube.

The use of elastomeric media has further advantages. The need for an elaborate control system to co-ordinate the axial compression with the hydraulic pressure is eliminated. Frictional forces between the tube and the elastomer are used to generate the axial compression, and the flexible medium applies a lateral pressure to the tube causing it to expand within the die. Moreover, the friction acting on the tube has an advantage in delaying the onset of tensile instability. When bulging with solid medium, sealing problems and the possibility of leakage of the high-pressure liquid employed in hydraulic bulging are eliminated. The cost of producing the component is much less than using a specialized machine required for hydraulic bulging. The need for the filling and removal of oil or the cleaning of the bulged tube of oil after forming is eliminated. The insertion of the elastomer rod is both quick and convenient and the rod can be re-used again [2].

Many experimental studies concerning bulge forming are available in literature [3-4] and in recent years a significant number of finite element simulation studies have been detailed out [5-8]. Different theoretical models have also been developed for the process [9-11]. Mac Donald and Hashmi [5] developed a three-dimensional simulation of the manufacture of cross-branch components using a solid bulging medium. The effect of varying friction between the bulging medium and the tube was examined in their paper and the history of development of the bulge and stress conditions in the formed component were investigated.

Hwang and Lin [7] proposed a theoretical model to examine the plastic deformation behavior of a thin-walled tube during the bulge hydro-forming process in an open die. They considered non-uniform thinning in the free-bulged region and sticking friction between the tube and die. The analysis was followed by finite element simulation of the process using DEFORM and the relationship between the internal pressure and the bulge height of the tube was achieved. Yang et al. [8] investigated the effect of the loading path on the bulged shape and the wall thickness distribution of the tube using theoretical and FE models. Using their model, a reasonable range of the loading path for the tube bulge hydro-forming process was determined.

Thiruvarudchelvan [9, 10] developed a theoretical model based on the experimental friction analysis performed by Fakuda and Yamaguchi [12]. Using this model he could determine the initial yield pressure and the final forming pressure needed to bulge a tube. Boumaiza et al. [11] discussed the plastic instabilities of elasto–plastic tubes subject to internal pressure and developed a local necking criterion based on a modified Hill's assumption for localized necking. In all these studies, the FE and theoretical analysis based on a comprehensive analytical friction model which takes into account the local contact condition have been missed.

Ramezani et al. [2] developed a friction model for rubber-metal contact in tube bulge forming process using solid medium. They showed in their paper that the newly developed friction model is very effective in producing reliable FE simulations compared to a traditional Coulomb friction model. In the present work, this friction model is used in theoretical analysis of tube bulging process to examine its efficacy in developing analytical models for rubber forming processes. Based on the results of a friction model developed by Ramezani et al. [2, 13] and an analytical model developed by Thiruvarudchelvan [9], an analytical analysis is performed for the case of tube end bulging with polyurethane medium, followed by finite element simulation of an axisymmetric tube bulging operation using ABAQUS software. To evaluate the influence of the new friction model, theoretical and FE simulation results have been compared with each other and with experimental results from [4].

2 Static friction model

When two solids are squeezed together they will in general not make atomic contact everywhere within the apparent contact area and contact happens only on peak asperities of surfaces [14]. To model the contact between rough surfaces, it is necessary to determine the contact parameters between the pair of asperities carrying the load [15]. For two elastic spherical asperities which are loaded by a normal force F_n, Hertz theory [16] is the basic theory for specifying the radius of the contact circle, the pressure and the normal approach. For the case when a tangential force F_t is subsequently applied, the tangential displacement of asperities and the shear stress within the contact can be determined by Mindlin theory [17]. He considered a stick region in the centre of contact between a pair of asperities surrounded by an annulus area of micro-slip across the edge of the contact. Johnson [18] presented a solution for this micro-slip region.

Rubber materials exhibit both elastic and viscous resistance to deformation. The materials can retain the recoverable (elastic) strain energy partially, but they also dissipate energy if the deformation is maintained [13]. Viscoelastic materials behavior can be modeled using springs and dashpots connected in series and/or in parallel. A dashpot is connected in parallel with a spring in Figure 1. This is known as a Voigt element. If deformed, the force in the spring is assumed to be proportional to the elongation of the assembly, and the force in the dashpot is assumed to be proportional to the rate of elongation of the assembly. In this model, if a sudden tensile force is applied, some of the work performed in the assembly is dissipated in the dashpot while the remainder is stored in the spring.

A dashpot is connected in series with a spring is shown in Figure 1(b). This is called a Maxwell element. In this assembly, if a sudden tensile force is applied, it is the same in both the spring and the dashpot. The total displacement experienced by the element is the sum of the displacements of the spring and the dashpot. The response of rubber to changes in stress or strain is actually a combination of elements of both mechanical models (see, Figure 1(c)). The response is always time-dependent and involves both the elastic storage of energy and viscous loss.

The Standard Linear Solid (SLS) model (Figure 1(c)) gives a relatively good description of both stress relaxation and creep behavior. Stress relaxation is the time-dependent decrease in stress under constant strain at constant temperature. For the SLS model the generalized Hook's equation can be written as

$$\eta_d\, g_1 \dot{\varepsilon} + g_1 g_2\, \varepsilon = \eta_d\, \dot{\sigma} + (g_1 + g_2).\sigma \qquad (1)$$

where g_1, g_2 are the elasticity of springs, η_d is the viscosity of the dashpot, ε is the strain and σ is the stress.

By making the stress constant and equal to σ_0 in Eq. (1) and solving the differential equation with respect to the strain ε, we arrive at the creep compliance function $\varphi(t)$ as follows:

$$\varphi(t) = \frac{\varepsilon(t)}{\sigma_0} = \frac{1}{g_1} + \frac{1}{g_2}[1 - \exp(\frac{-t}{T_2})] \qquad (2)$$

where $T_2 = \dfrac{\eta_d}{g_2}$ is the retardation time.

Similarly, the stress relaxation function $\psi(t)$ can be obtained by taking the strain constant and equal to ε_0 in Eq. (1), resulting in

$$\psi(t) = \frac{\sigma(t)}{\varepsilon_0} = \frac{g_1}{g_1 + g_2}[g_2 + g_1 \exp(\frac{-t}{T_2})] \qquad (3)$$

where $T_2 = \dfrac{\eta_d}{(g_1 + g_2)}$ is the retardation time.

Surface roughness can be modeled as a composed set of spherical asperities which have the same radius and their heights following a statistical distribution, as for instance a Gaussian distribution (see, Figure 2). Three parameters are commonly used to describe a random rough surfaces model. The statistical parameters of the asperities are: the average asperity radius β (spherical shaped asperities), the asperity density n, and the standard deviation of the asperity heights σ_s. According to experiments reported by Greenwood and Williamson [19] most surfaces show a value in the range of 0.03-0.05 for the product $n\beta\sigma_s$.

Hui et al. [20] developed a theory for viscoelastic-rigid contacts under several loading conditions such as constant load test, load relaxation test and constant displacement rate test. In this theory, an exponentially distribution of asperities is considered and then an analytical solution is developed for the real contact area and the total normal load. In this paper, the case of a viscoelastic rough surface which is normally loaded against a rigid surface is considered.

2.1 *Normal loading of viscoelastic/rigid multi-asperity contact*

For a certain separation h the number of asperities in contact, the real contact area and the total load carried by the asperities can be calculated using the following equations. The number of asperities in contact at a certain separation is given by

$$n_c = A_n\, n \int_{\bar{h}}^{\infty} \theta(\bar{s})\, d\bar{s} \qquad (4)$$

where A_n denotes the nominal contact area, $\bar{s} = s/\sigma_s$ is the normalized asperity height, $\bar{h} = h/\sigma_s$ is the normalized separation, and $\theta(\bar{s})$ is the normalized Gaussian height distribution which can be obtained as

$$\theta(\bar{s}) = \frac{1}{\sqrt{2\pi}}\, e^{-\frac{\bar{s}^2}{2}} \qquad (5)$$

Then, the real contact area is given by:

$$A_r = A_n\, n \beta \sigma_s\, \pi \int_{\bar{h}}^{\infty} (\bar{s} - \bar{h})\, \theta(\bar{s})\, ds \qquad (6)$$

The total normal load can be obtained as the sum of all normal loads carried by the asperities in contact.

$$F_n = A_n\, n \beta^{\frac{1}{2}} \sigma_s^{\frac{3}{2}} \frac{8}{3} \frac{1}{\varphi(t)} \int_{\bar{h}}^{\infty} (\bar{s} - \bar{h})^{\frac{3}{2}}\, \theta(\bar{s})\, d\bar{s} \qquad (7)$$

2.2 *Tangential loading of viscoelastic/rigid multi-asperity contact*

Considering the multi-asperity contact introduced in Section 2.1 to be subsequently loaded by an increasing tangential load, an approach is presented in this section for a viscoelastic rough surface pressed against a rigid flat.

At a certain separation and for a tangential load smaller than the force necessary to initiate macro-sliding, so-called maximum static friction force, the multi-contact interface will be composed of micro-contacts which are in the partially-slip regime and micro-contacts which are totally sliding. Macro-sliding will occur if all contacting asperities are in the fully sliding regime [17].

A condition has been set for an elastic multi-contact interface by Bureau et al. [21] which provides a critical asperity height above which the micro-contacts are partially sliding. In their approach, a constant local coefficient of friction is considered for all micro-contacts. Using Bureau method, a critical asperity height for a viscoelastic multi-contact interface can be derived.

$$\delta_{tv}(t) = \delta_n(t)\,\mu\,(2-\nu)\,[1-(1-\frac{F_t}{\mu.F_n})^{\frac{2}{3}}] \quad (8)$$

where δ_{tv} is the preliminary displacement; ν is the Poisson's ratio; and μ is the local coefficient of static friction. Rearranging the factors in Eq. (8), we arrive at:

$$1-\frac{\delta_{tv}(t)}{\delta_n(t)\,\mu\,(2-\nu)} = (1-\frac{F_t}{\mu.F_n})^{\frac{2}{3}} \quad (9)$$

The right-hand side of Eq. (9) is a positive real number for $F_t \le \mu.F_n$, thus:

$$\frac{\delta_{tv}(t)}{\mu\,(2-\nu)} \le \delta_n(t) \quad (10)$$

The indentation depth of the asperity δ_n can be replaced by $(z-h)$. Then, the inequality (10) becomes

$$z \ge \frac{\delta_{tv}(t)}{\mu\,(2-\nu)} + h \quad (11)$$

From Eq. (11) it can be inferred that the asperities which have the height

$$s_c \le \frac{\delta_{tv}(t)}{\mu\,(2-\nu)} + h \quad (12)$$

are in the fully sliding regime because they carry a tangential force which is equal to or larger than the maximum static friction force. The micro-contacts of which heights satisfy the relation $z \ge s_c$ are in the partially-slip regime.

The total tangential load carried by the multi-contact interface can be written as:

$$F_t = F_{stick} + F_{slip} \quad (13)$$

where F_{stick} component is calculated as the sum of all tangential loads carried by the micro-contacts which are not fully sliding. That means that their contact areas are composed of stick and slip regions. Deladi [22] presented the following equation for F_{stick} component:

$$F_{stick}(t) = A_n\, n\sigma_s^{\frac{3}{2}}\, \frac{8}{3}\, \frac{1}{\varphi(t)}\, \beta^{\frac{1}{2}} \times \int_{\bar{s}_c}^{\infty} (\bar{s}-\bar{h})^{\frac{3}{2}}\, \theta(\bar{s})\, \mu \left[1-\left(1-\frac{\delta_t}{(2-\nu)\,(\bar{s}-\bar{h})\,\mu\,\sigma_s}\right)^{\frac{3}{2}}\right] d\bar{s} \quad (14)$$

The F_{slip} component is taken as the sum of all tangential loads carried by the micro-contacts which are fully sliding and is calculated with equation

$$F_{slip}(t) = A_n\, n\sigma_s^{\frac{3}{2}}\, \frac{8}{3}\, \frac{1}{\varphi(t)}\, \beta^{\frac{1}{2}} \times \int_{\bar{h}}^{\bar{s}_c} (\bar{s}-\bar{h})^{\frac{3}{2}}\, \theta(\bar{s})\, \mu\, d\bar{s} \quad (15)$$

Having obtained the tangential load carried by the multi-contact interface, the maximum force required to initiate macro-sliding (or maximum static friction force) can be determined as the sum of all tangential loads causing gross sliding of all micro-contacts [22]. When this condition is obeyed, the partially sliding component F_{stick} becomes zero and the condition can be written as:

$$F_{st\max} = F_{slip} \quad if \quad F_{stick} = 0 \tag{16}$$

So, the static coefficient of friction can be calculated as:

$$\mu_s = \frac{F_{st\max}}{F_n} \tag{17}$$

By giving the micro-geometry, the nominal area of contact and the material properties, the real area of contact, A_r and the normalized separation, $\bar{h}$ can be obtained from Eqs. (6) and (7). Next, assuming a tangential displacement, the critical height, s_c can be calculated from Eq. (12). Then, the tangential loads carried by each micro-contact are obtained from Eqs. (14) and (15). If the partially stick component of the tangential force is not zero, the tangential displacement should be increased until all micro-contacts are fully sliding. This maximum tangential displacement corresponding to the occurrence of macro-sliding is taken as the global limiting displacement. At this stage, the maximum static friction force is reached and so, the static coefficient of friction is determined from Eq. (17).

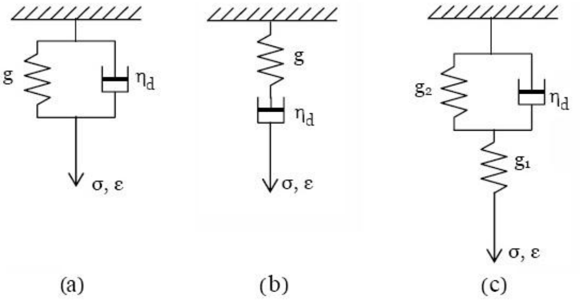

Figure 1: Mechanical models representing the response of viscoelastic materials: (a) Voigt model, (b) Maxwell model, (c) SLS model.

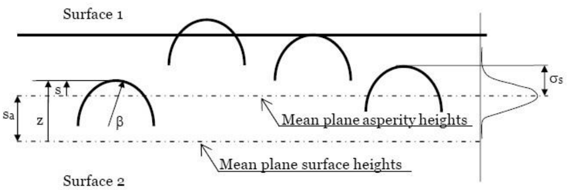

Figure 2: Contact model of rough surfaces.

2.3 *Calculation of friction coefficient*

An Alicona imaging infinite focus microscope (IFM 2.1) was used to measure the surface parameters of polyurethane. Surface parameters in terms of density of asperity n, mean radius of asperity β, and standard deviation of the asperity heights σ_s are the input parameters of the friction model. Figure 3 shows the roughness profile along a selected line in the surface. The geometrical parameters mentioned above can be obtained by these measurements using the Alicona microscope.

The viscoelastic material parameters in terms of spring elasticity g_1, g_2 and dashpot viscosity η_d of the SLS model are the other input parameters of the friction model. The values of viscoelastic material parameters used in the calculations of the friction model are obtained from a stress relaxation test of rubber. In a stress relaxation test a compressive strain at a constant rate within a very brief period of time is applied on an unconstrained cylinder and the stress required maintaining the compressive strain is recorded in time. The test is performed according to ASTM D 6048 standard. Stress relaxation modulus as a function of time (see, Eq. 3) for polyurethane of Shore hardness A 95 is shown in Figure 4. According to Eqs. (2) and (3), for $t \to 0$ we obtain $\psi(0) = \varphi(0)^{-1} = g_1$ and for $t \to \infty$ we have $\varphi(\infty) = \psi(\infty)^{-1} = \dfrac{g_1 + g_2}{g_1 . g_2}$. The values of input parameters for calculation of the coefficient of friction as a function of contact pressure are presented in Table 1.

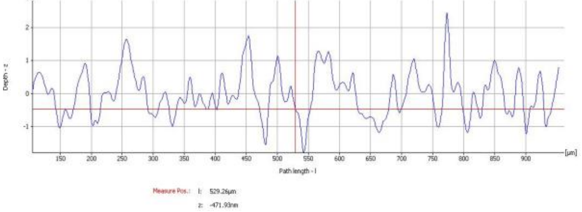

Figure 3: Roughness profile for polyurethane.

Using the values of parameters in Table 1 as input values for the friction model presented in Section 2, we calculated the coefficient of friction between polyurethane and copper tube as a function of contact pressure (see, Figure 5). It can be seen from Figure 5 that an increase in contact pressure results in decrease in coefficient of friction. At low pressures this decrease is more significant than at higher loads when the coefficient of friction reaches a quite stable level. This is comparable to the observation made by Benabdallah [23] where experimental work on some thermoplastics against steel and aluminum showed similar effect.

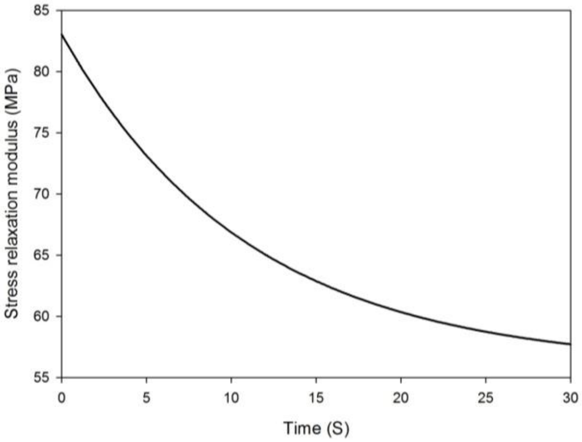

Figure 4: Stress relaxation modulus as a function of time for polyurethane rubber.

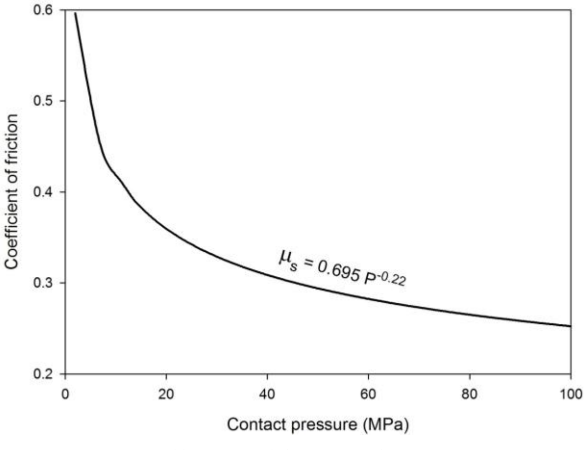

Figure 5: Coefficient of friction (for polyurethane/ copper contact) as a function of contact pressure.

The physical explanation for the increasing friction coefficient at lower pressures is that the effect of the adhesion force becomes more significant at lower normal loads [24]. High adhesion force decreases the separation h, at a given normal load and brings more asperities into contact especially when the normal load is small, enabling support for larger tangential load, and hence, the friction force and friction coefficient increase with decreasing normal load. From Figure 5 the following equation for the variation of coefficient of friction μ_s with pressure P is curve-fitted.

$$\mu_s = 0.695\, P^{-0.22} \tag{18}$$

Table 1: Values of the input parameters for friction model.

Parameters	Values
$n\ (m^{-2})$	2.7×10^{11}
$\beta\ (\mu m)$	0.542
$\sigma_s\ (\mu m)$	0.28
$g_1\ (Pa)$	8.30×10^{7}
$g_2\ (Pa)$	1.89×10^{-8}
$\eta_d\ (Pa.s)$	2.68×10^{9}
μ	0.4

3 Theoretical model

The schematic of tube bulge forming is shown in Figure 6. As can be seen in the figure, the tube and the polyurethane rod are divided into two zones (i.e. 0-1 and 1-2) to simplify the theoretical analysis. The tube is in full contact with the die wall in zone 0-1 and there is no plastic deformation of tube in this region. However, the tube is not constrained circumferentially in zones 1-2 and can deform plastically until taking the shape of the die. The theoretical model presented in this section is based on the work of Thiruvarudchelvan [9]. Mathematical formulations for the pressure in the polyurethane rod and stress components in the tube are developed for each zone and are presented below.

Zone 0-1:

According to Figure 6, the equilibrium equation for polyurethane rod at zone 0-1 can be expressed as

$$\mathrm{d}p \times \frac{\pi d^2}{4} = -\mu_s\, p\, \pi\, d\, \mathrm{d}x \tag{19}$$

Substituting Eq. (18) into Eq. (19) and simplifying the result, we arrive at

$$p^{-0.78}\,\mathrm{d}p = \frac{-4\times 0.695}{d}\,\mathrm{d}x \tag{20}$$

By integrating Eq. (20), we will have

$$p^{0.22} = -0.88\times 0.695\,\frac{x}{d} + C = -0.612\,\frac{x}{d} + C \tag{21}$$

According to Figure 6 at $x = 0$ we have $p = p_0$ and so $p_0^{0.22} = C$. Therefore

$$p = \sqrt[0.22]{\left(p_0^{0.22} - 0.612\,\frac{x}{d}\right)} \tag{22}$$

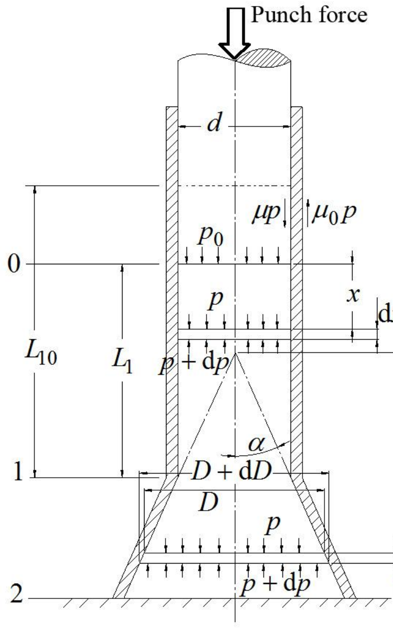

Figure 6: Schematic of tube bulge forming process.

On the other hand, the compressive axial load on the tube exerted by the polyurethane frictional force can be expressed as

$$F_x = \frac{\pi d^2}{4}(p_0 - p) \tag{23}$$

As the tube is dragged to the die surface, the frictional force exerted on the tube from the die is

$$F_F = \mu_0 \int_0^x p\,\pi\,d\,\mathrm{d}x = \mu_0\,\pi\,d \int_0^x \sqrt[0.22]{\left(p_0^{0.22} - \frac{0.612\,x}{d}\right)}\,\mathrm{d}x \tag{24}$$

Integrating Eq. (24) leads to

$$F_F = \mu_0\,\pi\,d \times \frac{0.22\times d}{0.612\times 1.22}\left(p_0^{1.22} - p^{1.22}\right) \tag{25}$$

where μ_0 is the coefficient of friction between the die and the tube. The axial compressive stress and the hoop stress on the tube wall in zone 0-1 can now be easily derived from Eqs. (22), (23) and (25) by using the following equations:

$$\sigma_x = \frac{F_x - F_F}{\pi\,d\,T} = \frac{d}{4T}\left[p_0 - \sqrt[0.22]{\left(p_0^{0.22} - \frac{0.612x}{d}\right)}\right] - \frac{0.295\,d\,\mu_0}{T}\left(p_0^{1.22} - p^{1.22}\right) \tag{26}$$

$$\sigma_\theta = \frac{p\,d}{2T} = \frac{d}{2T}\left[\sqrt[0.22]{\left(p_0^{0.22} - \frac{0.612x}{d}\right)}\right] \tag{27}$$

As the tube is completely surrounded by the die wall at zone 0-1, the hoop stress σ_θ is small and may be neglected. For this region and by neglecting the lateral pressure p, the Tresca yield criterion is $\sigma_\theta + \sigma_x = 1.1\,\sigma_0$, where σ_0 is the initial yield stress of the tube material. Thus

$$\sigma_\theta + \sigma_x = \frac{d}{4T}\left[p_0 + \sqrt[0.22]{(p_0^{0.22} - \frac{0.612x}{d})}\right] - \frac{0.295\,d\,\mu_0}{T}\left(p_0^{1.22} - p^{1.22}\right) = 1.1\,\sigma_0 \tag{28}$$

Zone 1-2:

The axial equilibrium equation for the polyurethane rod at zone 1-2 can be expressed as

$$\frac{\pi(D+\mathrm{d}D)^2}{4}(p+\mathrm{d}P) - \frac{\pi D^2}{4}\,p = \pi D\,\frac{p\,\mathrm{d}x}{\cos\alpha}(\sin\alpha - \mu_s\cos\alpha) \tag{29}$$

By neglecting higher order terms of Eq. (29) and rearranging the equation, we have

$$(2p\,\mathrm{d}D + D\,\mathrm{d}p) = 4p\frac{\mathrm{d}D}{2\tan\alpha}(\tan\alpha - \mu) \qquad (30)$$

Considering $\mathrm{d}x = \mathrm{d}D/2\tan\alpha$, we have

$$\frac{\mathrm{d}D}{D} = -\frac{\mathrm{d}p}{2\mu_s\, p\cot\alpha} = -\frac{\mathrm{d}p}{1.39\, p^{0.78}\cot\alpha} \qquad (31)$$

Integrating Eq. (31) leads to

$$\ln D + \frac{50}{11\times 1.39\cot\alpha}\, p^{0.22} + C = 0 \qquad (32)$$

According to Figure 6 at $D = d$ we have $p = p_1$ and so $\left(-\ln d - \frac{3.27}{\cot\alpha}\, p_1^{0.22}\right) = C$. Therefore

$$p = \sqrt[0.22]{\left(p_1^{0.22} - 0.306\ln\frac{D}{d}\cot\alpha\right)} \qquad (33)$$

Neglecting the effect of bending at point 1, the equilibrium equation normal to the conical surface of the tube at zone 1-2 is

$$\frac{\sigma_\theta\cos\alpha}{r} = \frac{p - p_d}{T} \qquad (34)$$

where σ_θ is the tensile hoop stress. Assuming constant thickness, the equilibrium equation along the axis of the tube is

$$T\cos\alpha\frac{\mathrm{d}(\sigma_\alpha\, r)}{\mathrm{d}r} = (p_d - p)r + \mu_s\, p\cot\alpha - \mu_0\, p_d\cot\alpha \qquad (35)$$

Combining Eqs. (34) and (35) leads to

$$\left(r\,\mathrm{d}\sigma_\alpha + \sigma_\alpha\,\mathrm{d}r\right) = \left[-\sigma_\theta + (\mu_s\, p - \mu_0\, p_d)\frac{\cot\alpha}{T\cos\alpha}\right]\mathrm{d}r \qquad (36)$$

where σ_θ and σ_α are tensile and compressive stresses respectively. Using the modified Tresca yield criterion $\sigma_\theta + \sigma_\alpha = 1.1\,\sigma_m$ and combining Eqs. (34) and (36) lead to

$$\mathrm{d}\sigma_\alpha + \mu_0\,\sigma_\alpha\cot\alpha\frac{\mathrm{d}r}{r} = 1.1\sigma_m(\mu_0\cot\alpha - 1)\frac{\mathrm{d}r}{r} + \frac{\operatorname{cosec}\alpha}{T}(0.695\, p^{0.78} - \mu_0\, p)\,\mathrm{d}r \qquad (37)$$

where σ_m is the average yield stress of the tube material. By integrating and manipulating Eq. (37), we arrive at the following expression for the compressive meridian stress in section 2 ($r = r_2$):

$$\begin{aligned}\sigma_{\alpha 2} = {} & \left(\frac{d}{D}\right)^{(\mu_0\cot\alpha)}\sigma_{\alpha 1} + 1.1\sigma_m\left(\frac{\mu_0\cot\alpha - 1}{\mu_0\cot\alpha}\right)\left[1 - \left(\frac{d}{D}\right)^{(\mu_0\cot\alpha)}\right] \\ & + \frac{0.695\operatorname{cosec}\alpha}{T(D/2)^{(\mu_0\cot\alpha)}}\int_{r_1}^{r_2}\left(p_1^{0.22} - 0.306\cot\alpha\ln\frac{r}{r_1}\right)^{3.55} r^{(\mu_0\cot\alpha)}\,\mathrm{d}r \\ & - \frac{\mu_0\operatorname{cosec}\alpha}{T(D/2)^{(\mu_0\cot\alpha)}}\int_{r_1}^{r_2}\left(p_1^{0.22} - 0.306\cot\alpha\ln\frac{r}{r_1}\right)^{4.55} r^{(\mu_0\cot\alpha)}\,\mathrm{d}r\end{aligned} \qquad (38)$$

Calculation procedure:

From the above calculations, the pressures at sections 1 and 2 are given by Eqs. (22) and (33), respectively.

$$\begin{aligned} p_1 &= \sqrt[0.22]{\left(p_0^{0.22} - 0.612\frac{L_1}{d}\right)} \\ p_2 &= \sqrt[0.22]{\left(p_1^{0.22} - 0.306\ln\frac{D}{d}\cot\alpha\right)}\end{aligned} \qquad (39)$$

Also, the compressive meridian stresses at sections 1 and 2 can be achieved by Eqs. (26) and (38), respectively.

$$\sigma_1 = \frac{d}{4T}(p_0 - p_1) - \frac{0.295\, d\,\mu_0}{T}\left(p_0^{1.22} - p_1^{1.22}\right) \qquad (40)$$

$$\begin{aligned}\sigma_2 = {} & \left(\frac{d}{D}\right)^{(\mu_0\cot\alpha)}\sigma_1 + 1.1\sigma_m\left(\frac{\mu_0\cot\alpha - 1}{\mu_0\cot\alpha}\right)\left[1 - \left(\frac{d}{D}\right)^{(\mu_0\cot\alpha)}\right] \\ & + \frac{0.695\operatorname{cosec}\alpha}{T(D/2)^{(\mu_0\cot\alpha)}}\int_{r_1}^{r_2}\left(p_1^{0.22} - 0.306\cot\alpha\ln\frac{r}{r_1}\right)^{3.55} r^{(\mu_0\cot\alpha)}\,\mathrm{d}r \\ & - \frac{\mu_0\operatorname{cosec}\alpha}{T(D/2)^{(\mu_0\cot\alpha)}}\int_{r_1}^{r_2}\left(p_1^{0.22} - 0.306\cot\alpha\ln\frac{r}{r_1}\right)^{4.55} r^{(\mu_0\cot\alpha)}\,\mathrm{d}r\end{aligned} \qquad (41)$$

The initial pressure exerted on the top of the polyurethane rod to bulge the tube, p_0 can be obtained from FE simulations and subsequently, the values of p_1, p_2 and σ_1, σ_2 can be calculated using Eqs. (39-41).

4 Finite element simulation

Numerical studies were carried out to reveal the deformation pattern of the tube and to verify the theoretical analysis. A range of forming parameters can be used in the finite element simulations and the optimal values can be predicted at low CPU cost.

ABAQUS finite element code was used to simulate the process and predict the material deformation during forming. Due to the axisymmetric character of the forming, only a 2-D model was used to reduce computation time. Figure 7 shows the shape at the last stage of the tube bulging using a solid bulging medium. A polyurethane rod of Shore Hardness 95A and diameter 38*mm* was used to bulge an annealed copper tube of diameter 42*mm* and wall thickness of 1.2*mm*. The bottom plate of the die was not modeled, instead the nodes at the bottom of die, tube and flexible medium were constrained in the appropriate directions to simulate the presence of the die bottom plate.

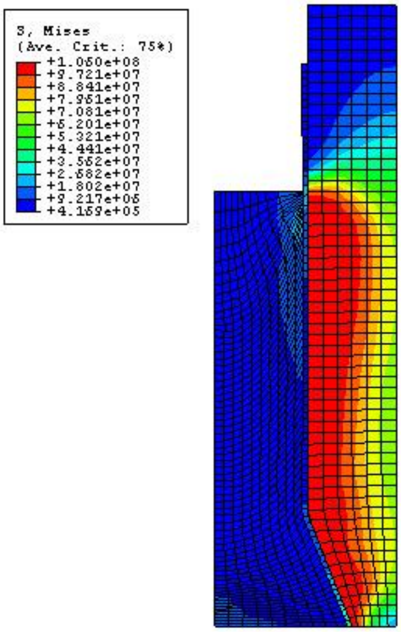

Figure 7: FE simulation of the process at the last stage of bulge forming.

Die tool material was assumed to be steel, and the tube was modeled using CAX4R (a 4-node bilinear axisymmetric quadrilateral, reduced integration, hourglass control) elements. The polyurthane rod was modeled using CAX4RH elements. Penalty contact interfaces were used to enforce the intermittent contact and the sliding boundary condition between the blank and the tooling elements. The Coulomb friction model with various values of coefficient of friction is used for contact surfaces between the tube and the metallic die. The coefficient of friction between the polyurethane and the tube changes with contact pressure based on the model presented in section 2. The contact pressure dependent coefficients of friction are implemented into the model through the contact property option of the ABAQUS program. This option is used to introduce friction properties into the mechanical surface interaction models.

The simulation begins with the tube in contact with the die and the polyurethane rod. The flexible rod then moves down to bulge the tube. The interface between the die and the tube, and between the tube and the flexible rod are modeled using an automatic surface to surface contact algorithm. The forming loads were applied on the polyurethane rod in terms of displacements on the top surface of the rod. The displacement was assigned to be equal to the displacement of the rod measured during the experimental tests performed by Girard et al. [4].

The constitutive behavior of the tube is described by an elastic–plastic model. For the elastic part, Young's modulus of 110*GPa* and Poisson's ratio of 0.343 is used. For the plastic part, the hardening model is assumed to be isotropic described by the power law approach:

$$\sigma = K\,\varepsilon^{n} \tag{42}$$

where σ is the true stress (MPa), ε is the total true strain (dimensionless), K is the strength coefficient (MPa) and n is the strain-hardening exponent (dimensionless). For the annealed copper in this research, $K = 530\ MPa$ and $n = 0.44$ are being used and the average yield stress of the annealed copper is $\sigma_m = 97MPa$.

Rubber is made of isotropic, non-linear, hyper-elastic, incompressible, strain-history-independent material. Hyper-elastic materials are described in terms of a strain energy potential W which defines the strain energy stored in the material per unit of reference volume (volume in the initial configuration) as a function of the strain at that point in the material

[25]. Among several forms of strain energy potentials available in ABAQUS, Ogden (N=3) strain energy [26] is used for rubber modeling. The Ogden material model has previously been used with success to predict the behavior of hyper-elastic materials at high strain rates (see, e.g. [27]). The form of the Ogden strain energy potential is:

$$\sigma_{ij} = \frac{\partial W}{\partial \varepsilon_{ij}} \tag{43}$$

$$W = \sum_{i=1}^{N} \frac{2\mu_i}{\alpha_i^2}(\bar{\lambda}_1^{\alpha_i} + \bar{\lambda}_2^{\alpha_i} + \bar{\lambda}_3^{\alpha_i} - 3) + \sum_{i=1}^{N} \frac{1}{D_i}(J^{el} - 1)^{2i} \tag{44}$$

where W is the strain energy per unit of reference volume; $\bar{\lambda}_i$ are the deviatoric principal stretches which can be defined by $\bar{\lambda}_i = J^{-1/3}\lambda_i$; λ_i are the principal stretches; J is the total volume ratio; J^{el} is the elastic volume ratio; and μ_i, α_i and D_i are temperature-dependent Ogden constants. Compressibility can be defined by specifying nonzero values for D_i, by setting the Poisson's ratio to a value less than 0.5, or by providing test data that characterize the compressibility. We assumed a fully incompressible behavior for rubber with $\nu = 0.4997$ and D_i equal to zero and so the second expression in Eq. (44) can be eliminated. To determine the strain energy density W, ABAQUS uses a least-squares fitting algorithm to evaluate the Ogden constants automatically from experimental data.

5 Results and discussions

To validate the FE model developed in Section 4, the final thickness of the tube after bulging is compared with experimental results presented by Girard et al. [4] and is shown in Figure 8. As demonstrated in the figure, the thickness distribution obtained from the FE model and the experiments agree very well with each other with the error less than 6%. As shown in the figure, the maximum thinning happens at the end of the tube, where the tube has the maximum expansion. The undeformed part of the tube does not show any reduction in thickness.

The pressure P_0 at the top of the polyurethane rod obtained from FE simulations with different values of coefficient of friction between the die and the tube is shown in Figure 9. As can be seen in the figure, higher pressures are needed for bulging with higher friction coefficients to overcome the frictional resistance between the die and the tube.

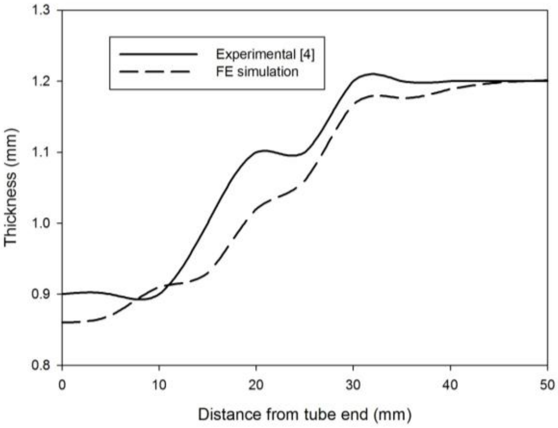

Figure 8: Thickness distribution of the bulged tube obtained from FE simulations.

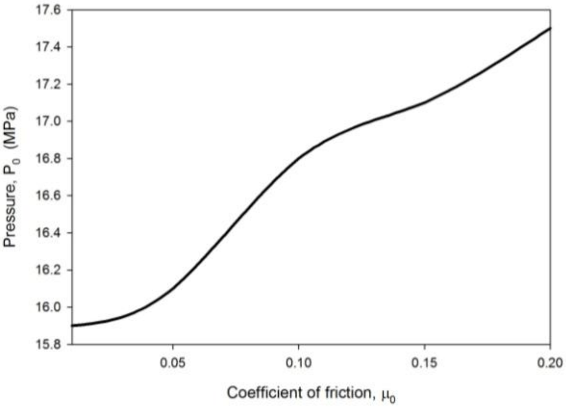

Figure 9: Pressure at the top of the polyurethane rod obtained from FE simulations.

The variations of pressures at points 1 and 2 (see Figure 6) of the rod are illustrated in Figures 10 and 11. The values of P_1 and P_2 are calculated using Eq. (39). According to the figures, the results of FE simulations and the theoretical model correlate with each other. The maximum error for predicting P_1 is

4.6% which happens at the coefficient of friction of 0.1. The error increases to 4.9% for prediction of P_2.

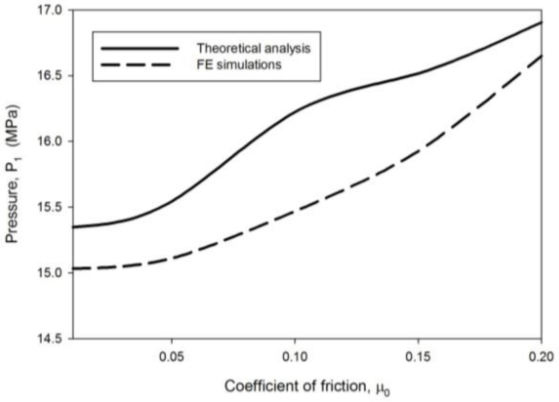

Figure 10: Variation of P_1 with coefficient of friction.

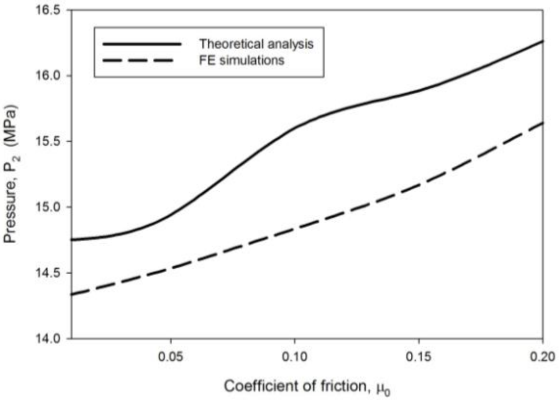

Figure 11: Variation of P_2 with coefficient of friction.

The effect of tube initial thickness and length of the rod on the distribution of pressure at different points of the polyurethane rod is calculated using the theoretical model and presented in Figures 12 and 13. As can be seen in the Figure 12, higher pressures are needed to bulge the tubes with thicker walls. Figure 13 shows that as length of the rod in contact with the constrained part of the tube increases, the pressure needed to bulge the tube increases. However, the calculations show that the effect of rod length is not as significant as the tube thickness.

The effect of coefficient of friction between the tube and the die on the variations of stresses σ_1 and σ_2 at points 1 and 2 of the tube (see Figure 6) is shown in Figures 14 and 15. It can be seen that the stress components tend to increase with increasing the coefficient of friction. This is due to the higher forming pressure exerted to the tube from the polyurethane rod at higher frictions. The theoretical model predicts this increase quite linearly. The comparisons between the theoretical and FE simulation results show good correlation. The maximum prediction error at $\mu_0 = 0.2$ is 12% for σ_1 and 8.2% for σ_2. The FE simulations tend to predict the stresses higher than the theoretical model.

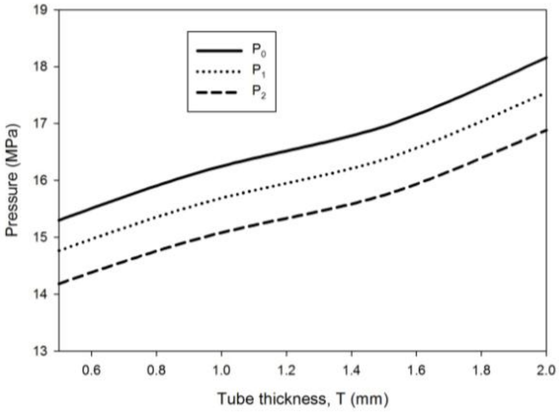

Figure 12: Variation of pressures at different points of the polyurethane rod with tube thickness.

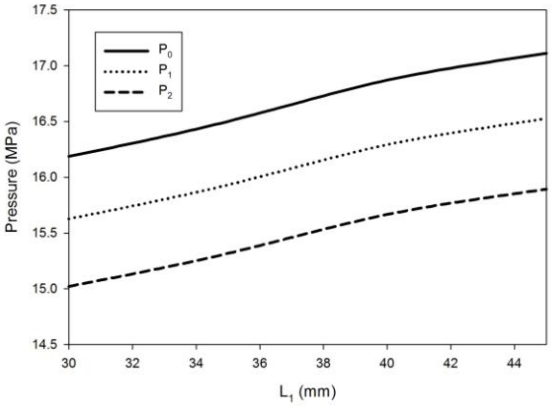

Figure 13: Variation of pressures at different points of the polyurethane rod with the length of the rod.

Effects of initial tube thickness and polyurethane rod length on the stress at point 2 of the tube are calculated using the theoretical model and are shown in Figures 16 and 17. As demonstrated in Figure 16, the stress at point 2 increases sharply with decreasing the initial tube thickness which makes it difficult to bulge very thin tubes. According to Figure 17, the increase in the rod length does not have a remarkable effect on the stress at point 2.

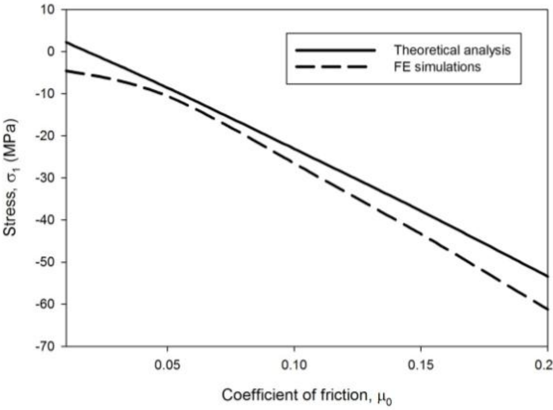

Figure 14: Variation of stress σ_1 with coefficient of friction.

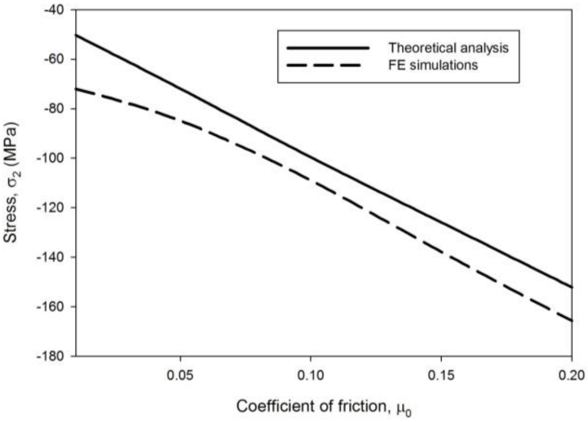

Figure 15: Variation of stress σ_2 with coefficient of friction.

The history of radial stress at points 1 and 2 during the FE simulation is shown in Figure 18. As shown in the figure, the compressive radial stress increases constantly during the process and makes it possible to expand and bulge the tube end. The values of stresses at points 1 and 2 are quite similar which is due to the hydrostatic nature of the bulge forming using an elastomer bulging medium. The variation of axial stress at points 1 and 2 of the tube with simulation time is shown in Figure 19. As can be seen in the figure, the axial stresses increase with time, however there is a sharp decrease in axial stress at point 1 at the end stages of the bulge forming process.

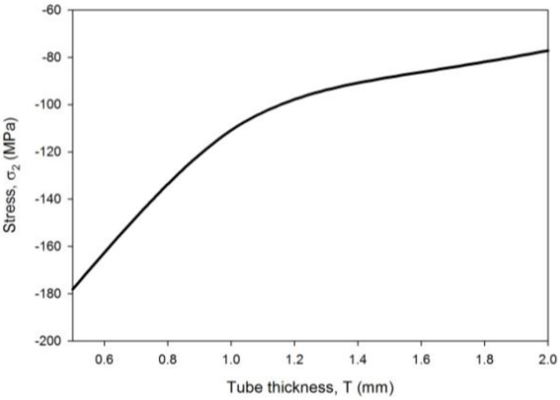

Figure 16: Effect of initial tube thickness on stress σ_2.

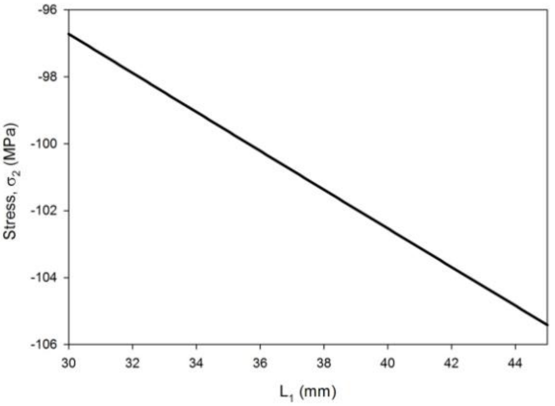

Figure 17: Effect of polyurethane rod length on stress σ_2.

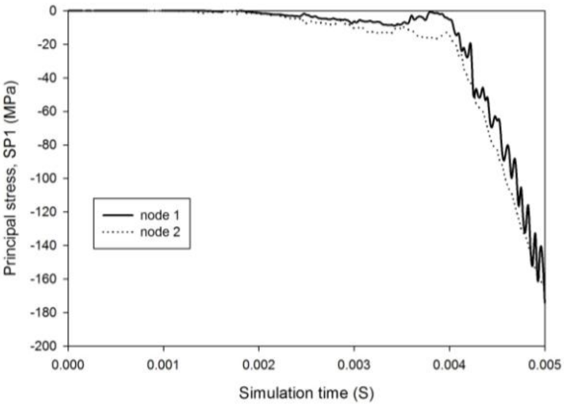

Figure 18: Radial stress history at point 1 ad 2 of the tube during bulging simulation.

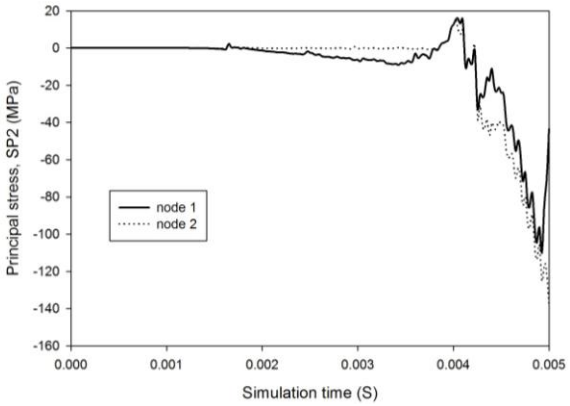

Figure 19: Axial stress history at point 1 ad 2 of the tube during bulging simulation.

6 Conclusions

In this paper bulge forming of tubular components was investigated using an analytical model and FE simulations. A new friction model based on local contact conditions was used in the FE simulation of the process and based on the results of this friction model, a theoretical model for bulge forming was developed. The main conclusions of this research are as follows:

- An increase in contact pressure results in decrease in coefficient of friction between rubber and metal. The coefficient of friction reaches a nearly constant value at higher normal pressures.
- Higher pressures are needed to bulge the tubes with thicker walls. The stress at the end of the tube increases sharply with decreasing the initial thickness of the tube, which may cause rupture at the end of the tubes with very thin walls.
- The effect of the length of the elastomeric rod on the pressure and stress distributions is negligible.
- Compressive axial and radial stresses at the tube increase constantly during the process which makes it possible to bulge the tube.

References

[1] Mac Donald BJ, Hashmi MSJ (2002) Near-net-shape manufacture of engineering components using bulge-forming processes: a review. J Mater Process Technol 120:341–347.

[2] Ramezani M, Ripin ZM, Ahmad R (2009) A static friction model for tube bulge forming using a solid bulging medium. Int. J. Adv. Manuf. Tech. 43 (3–4):238–247.

[3] Kim J, Kim SW, Park HJ, Kang BS (2006) A prediction of bursting failure in tube hydroforming process based on plastic instability. Int J Adv Manuf Technol 27:518–524.

[4] Girard AC, Grenier YJ, Mac Donald BJ (2006) Numerical simulation of axisymmetric tube bulging using a urethane rod. J Mater Process Technol 172:346–355.

[5] Mac Donald BJ, Hashmi MSJ (2001) Three-dimensional finite element simulation of bulge forming using a solid bulging medium. Finite Elem Anal Des 37:107–116.

[6] Pipan J, Kosel F (2002) Numerical simulation of rotational symmetric tube bulging with inside pressure and axial compression. Int J Mech Sci 44:645–664.

[7] Hwang YM, Lin YK (2002) Analysis and finite element simulation of the tube bulge hydroforming process. J Mater Process Technol 125–126:821–825.

[8] Yang B, Zhang WG, Li SH (2006) Analysis and finite element simulation of the tube bulge hydroforming process. Int J Adv Manuf Technol 29 (5):453–458.

[9] Thiruvarudchelvan S (1994) A theory for the bulging of aluminum tubes using a urethane rod. J Mater Process Technol 41:311–330.

[10] Thiruvarudchelvan S (1994) A theory for initial yield conditions in tube bulging with a urethane rod. J Mater Process Technol 42:61–74.

[11] Boumaiza S, Cordebois JP, Brunet M, Nefussi G (2006) Analytical and numerical study on plastic instabilities for axisymmetric tube bulging. Int J Mech Sci 48:674–682.

[12] Fukuda M, Yamaguchi K (1974) On the coefficient of friction between rubber and metal under high pressure. Bulletin of JSME 17 (103):157–164.

[13] Ramezani M, Ripin ZM, Ahmad R (2009) Computer aided modelling of friction in rubber-pad forming process. J Mater Process Technol 209 (10):4925-4934.

[14] Ramezani M, Ripin ZM, Ahmad R (2008) Modelling of kinetic friction in V-bending of ultra-high-strength steel sheets. Int J Adv Manuf Technol 46 (1-4):101-110.

[15] Ramezani M, Ripin ZM (2010) A friction model for dry contacts during metal-forming processes. Int J Adv Manuf Technol 51 (1-4):93-102.

[16] Hertz H (1882) Über die Berührung fester elastischer Körper. J. Reine. Angew. Math. 92:156–171.

[17] Mindlin RD (1949) Compliance of elastic bodies in contact. ASME J. Appl. Mech. 16: 259–268.

[18] Johnson KL (1985) Contact mechanics. Cambridge: Cambridge University Press.

[19] Greenwood JA, Williamson JBP (1966) Contact of nominally flat surfaces. Proc. Roy. Soc. London, A 295:300–319.

[20] Hui CY, Lin YY, Baney JM (2000) The mechanics of tack: viscoelastic contact on a rough surface. J Polym Sci, B: Polymer Physics, 38:1485–1495.

[21] Bureau L, Caroli C, Baumberger T (2003) Elasticity and onset of frictional dissipation at a non-sliding multi-contact interface. Proc. Roy. Soc. London, A 459, 1183:27871–2805.

[22] Deladi EL (2006) Static friction in rubber–metal contacts with application to rubber pad forming processes. PhD thesis, University of Twente, The Netherlands.

[23] Benabdallah HS (2007) Static friction coefficient of some plastics against steel and aluminum under different contact conditions. Tribol. Int. 40:64–73.

[24] Yu N, Pergande SR, Polycarpou AA (2004) Static friction model for rough surfaces with asymmetric distribution of asperity heights. ASME J Tribol 126:626–629.

[25] Ramezani M, Ripin ZM, Ahmad R (2009) Numerical simulation of sheet stamping process using flexible punch. Proc. IMechE, B: J. Eng. Manuf. 223 (7):829-840.

[26] Ogden RW (1972) Large deformation isotropic elasticity–on the correlation of theory and experiment for incompressible rubberlike solids. Proc. Roy. Soc. London, A 326:565-84.

[27] Ramezani M, Ripin ZM (2010) Combined experimental and numerical analysis of bulge test at high strain rates using split Hopkinson pressure bar apparatus. J. Mater. Process. Tech. 210 (8):1061-1069.